Science Advances

MAAAS

Supplementary Materials for

Imperfect bodies sink imperfectly when settling in granular matter

Marcos Espinosa *et al.*

Corresponding author: Ernesto Altshuler, ealtshuler@fisica.uh.cu

The PDF file includes:

Figs. S1 to S8
Legends for movies S1 to S8

Other Supplementary Material for this manuscript includes the following:

Movies S1 to S8

DETAILS OF SAND PENETRATION EXPERIMENTS

As described in the main text, sand was fluidized by injecting air from the bottom in our first two experiments. The fluidization process involves bubbling, which is not easy to characterize. However, we attempted to visualize the bubbles and quantify their influence in the tilting of the intruders, as follows.
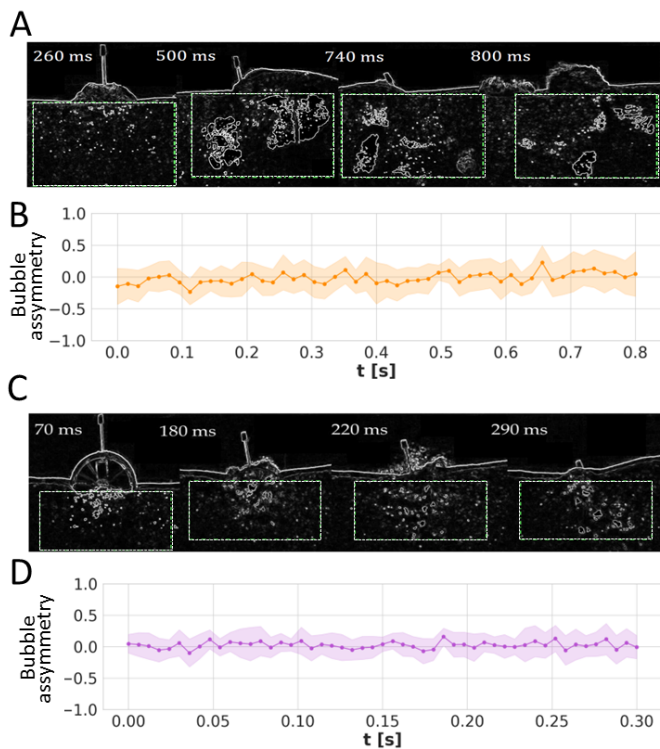

Fig. S1. Bubble visualization. (A) Four snapshots of the penetration of a stone into an air-fluidized bed. (B) Bubble area asymmetry relative to the a vertical axis passing by the stone's center of mass (see text for further details) as time goes by. (C) and (D) are analogous to (A) and (B), but for the case of the Janus cylinder. The discontinuous lines rectangles show the region where the bubbles' areas were calculated.

We first established an area of interest for bubble analysis, consisting in moving rectangles centered at the intruder's

*

center of mass of areas 21.78 cm^2 for the cylinder and 32 cm^2 for the rock (see dotted-line rectangles in the snapshots shown in Fig. S1 (A) and (C)). The well-known Canny algorithm (Song et al., [28]) was used to reveal the bubble shapes, and then the dilate and erode technique was used for isolation of individual bubbles (Ragnemalm, [29]). We checked by visual inspection that the resulting bubble contours coincided with the direct observation of the real video. Using the processed videos, we measured various parameters, like the number of bubbles in the area of interest, their average size, and their area.

While extracting a trustable relation between these parameters and the resistive force exerted by the granular medium against the intruder turns out to be extremely difficult, we were able to provide strong evidence supporting the lack of correlation between eventual bubbling asymmetries and the asymmetric tilting of the intruder. We did it by defining the Bubble Asymmetry as the the difference between the total bubble area at the left of the vertical axis passing by the center of mass of the intruder (A_l) and its analogous area at the right (A_r), divided by the total area, i.e. $(A_l - A_r)/(A_l + A_r)$. Its temporal evolution is shown for the sand-penetrating stone and Janus intruder in S1 (B) an (D), respectively. It becomes clear that there is no asymmetry in the bubbling of the granular bed around the intruders, which strongly suggests that it is not responsible for their systematic tilting, as declared in the main text.

However, it must be underlined that our analysis only included bubbles near the glass surface nearer to the camera, so our observations cannot be mechanically extrapolated to bubbling taking place far from the glasses.

So, the fact that when the intruder is flipped around an horizontal axis the tilt direction inverts (as described in the main text) is still a powerful argument indicating that the imperfections of the intruder itself control the dynamics.

FURTHER DEM SIMULATIONS

Using LAMMPS (Plimpton, [34]) to perform 2D simulations (following the protocols described in the Methods section of the main text) we reproduce the motion of a circular disk, of the same radius as the experimental cylinder, with a grain of diameter 0.007 m, attached to the surface of the intruder

at different angular positions: 30°, 60°, 90° relative to the downward direction, in addition to the $\theta = 15^o$ case discussed in the main text. Fig. S2 shows the ability of the simulations to reproduce at least semi-quantitatively the experimental results for Scarface intruders.
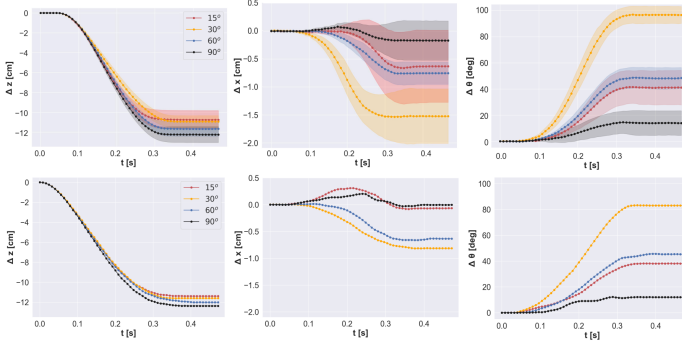

Fig. S2. DEM simulations reproduce experimental results for Scarface intruders. Top row: experimental results for 15°, 30°, 60°, 90° Scarface Janus intruders. From left to right: vertical penetration, horizontal penetration, and angular motion as a function of time. Bottom row: Two-dimensional DEM simulations reproducing the experimental results shown above.

The force exerted on the adhered grain was obtained by extracting from the simulations the average force of the grain-grain interaction at each time step ($\sim 2.82 \times 10^{-7}$ s). With this information we determined the average torque exerted by the granular material on the glued grain on a small time scale, which, as indicated in the main text, is responsible for the sudden variations of the intruder's motion. As described in the main text for the case of $\theta_{grain} = 15^o$, in Fig. S3 we see the great influence that the glued grain has on the rotation of the intruder. Our simulations adequately reproduce what is expected according to experimental observations: the torque should decrease for 60°, 90° with respect to 30°, which is clearly brought out in Fig. S3.

In order to validate the theoretical model presented in the main text, additional numerical simulations were conducted to examine the torque generated by the friction between the intruder and the free grains, as well as the torque exerted by the normal force on the attached grain. The results of the simulations are presented in Fig. S4, which demonstrates that the positive rotation of the intruder is primarily driven by the force transmitted by the glued grains. Meanwhile, the tangential force resulting from the interaction between the intruder and the granular bed only causes minimal dissipation.

DETAILS OF THE ANALYTICAL MODEL FOR THE SCARFACE JANUS CYLINDERS

Considering Katsuragi-Durian force law [10], and neglecting the inertial drag due to the slow-speed penetration dynamic, we have:

$$M\ddot{z}(t) = -Mg - kz(t) \qquad (1)$$

where k depends on the material properties of the granular bed and the intruder geometry. To model the penetration of the ScarFace intruder, we make the assumption that the attached
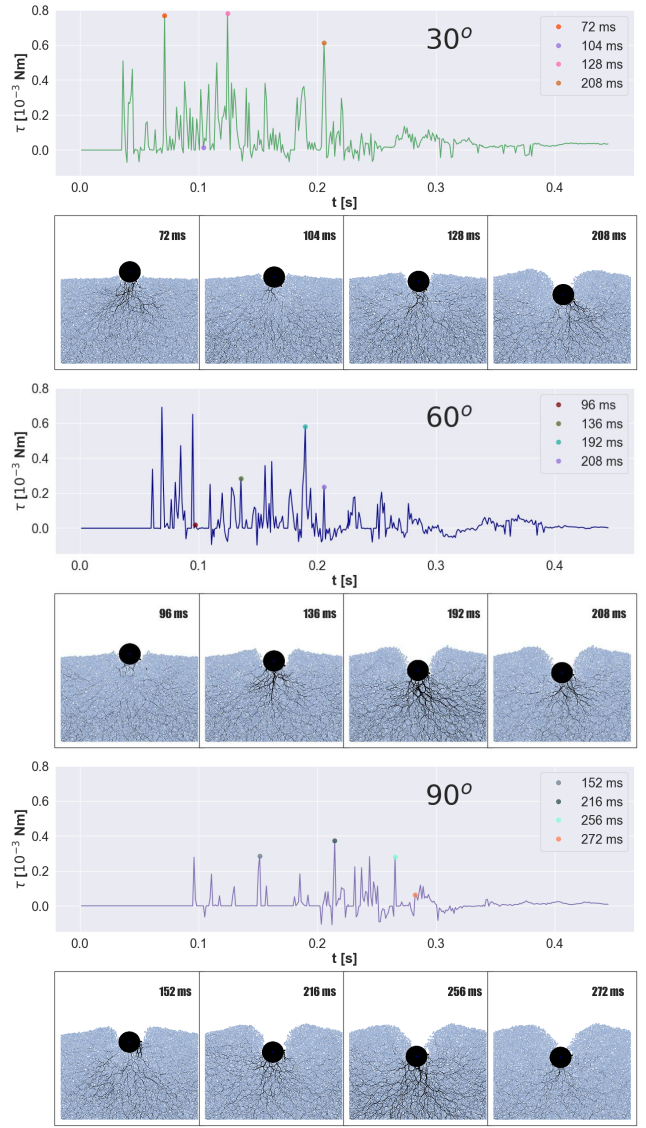

Fig. S3. Torques and force chains for 30°, 60°, 90° Scarface Janus intruders based in DEM simulations. Top panels: Time evolution of the torque on a single grain attached to the surface of a disk-shaped intruder at 30°, 60°, 90° relative to the downward direction, resulting from DEM simulations. Bottom panels: Four snapshots showing the force chains corresponding to peaks and valleys in the top panels (force strength is proportional to the thickness of the black lines)

grains exert a force, $\vec{F}_{gKD}$, onto the intruder. This force is hypothesized to be dependent on the vertical position of the attached grains, in accordance with the Katsuragi-Durian model, multiplied by a quadratic cosine function. Moreover, it is proposed that the orientation angle of $\vec{F}_{gKD}$ scales as $\frac{\theta}{4}$. This proportionality is based on the observation, demonstrated in Fig. S3, that granular force chains exhibit a decreased degree of verticality as their distance from the bottom of the intruder increases. For simplicity, we assume a 2D model of the intruder, meaning the grain row is modeled as a single circular particle. As the mass of the grain is much smaller than that of the intruder, the force acting on the grain can be approximated as:

$$F_{grain} \approx -kz_{grain}(t) \quad (2)$$

Where $z_{grain} = z - (R + r)\cos\theta$.

Based on the force diagram shown in Fig. 4 of the main text, we obtain:

$$M\ddot{z} = -Mg + F_{KD} + F_{gKD}\cos(\theta/4) \quad (3)$$
$$M\ddot{x} = -F_{gKD}\sin(\theta/4) \quad (4)$$
$$\frac{1}{2}MR^2\ddot{\theta} = F_{gKD}R\sin(3\theta/4), \quad (5)$$

where:

$$F_{KD} = -kz$$
$$F_{gKD} = -k[z - (R+r)\cos\theta]H(\theta - \theta_{max})\cos^2\left(\frac{\theta\pi}{2\theta_{max}}\right)$$
$$\theta_{max} = \frac{\pi}{2} + \cos^{-1}\left(1 - \frac{r}{R}\right)$$
$$\quad (6)$$

where we have not made explicit the time dependence of x, z and θ for space reasons. We posit that the behavior of F_{gKD} is described by expression (7) for two reasons. Firstly, the presence of the Heaviside step function accounts for the fact that when $\theta = \theta_{max}$, the attached grain is no longer in contact with force chains and therefore cannot affect the motion of the intruder, resulting in $F_{gKD} = 0$. Secondly, this expression takes into consideration the increased resistance to motion at the bottom of the intruder by incorporating the term $\cos^2(\frac{\theta(t)\pi}{2\theta_{max}})$. It is noteworthy that the resistive force acting on the intruder already decreases as $\theta(t)$ increases due to the change in the vertical position of the glued grains,

however, the rate of decrease was not in agreement with the values obtained from experiments and DEM simulations. The addition of the squared cosine function reduced the root-mean-square errors between the theoretical predictions and the experimental data (more than 30%).

To numerically solve the Eqs. 3-5, two more considerations were taken into account. The first is that we assume free-fall (only gravity acting on the intruder), until $z(t) = 0$, i.e, half of the intruder has penetrated into the granular bed. The second is that, when $v_z = 0$, we assume that the intruder *freezes* in its current position, i.e., all forces, torques and velocities are made zero. This approximation is used to avoid the bouncing of the intruder, resulting from the condition $kz > Mg$ when $v_z = 0$. In fact, it is a way to mimic the experimental situation: when the intruder stops the distribution of force chains is such that it equals the effect of gravity acting on the intruder (i.e $|kz|$ sharply decreases from a value higher than Mg to a value equal to Mg at the end of the trajectory). In fact, it is a method to simulate the experimental scenario: when $v_z = 0$, the intruder stops
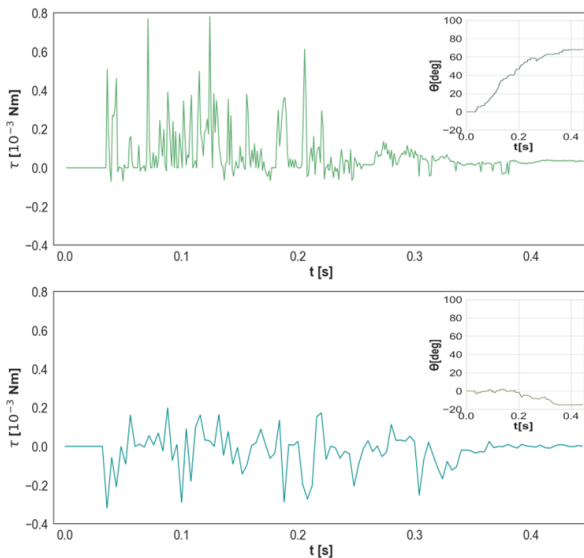

Fig. S4. Characterization of torques acting on the intruder, based on DEM simulations. Top: Torque generated by the normal force on the attached grain. Bottom: Torque resulting from tangential friction between the cylinder and granular bed. Insets show the rotational motion obtained through numerical integration of both torques.
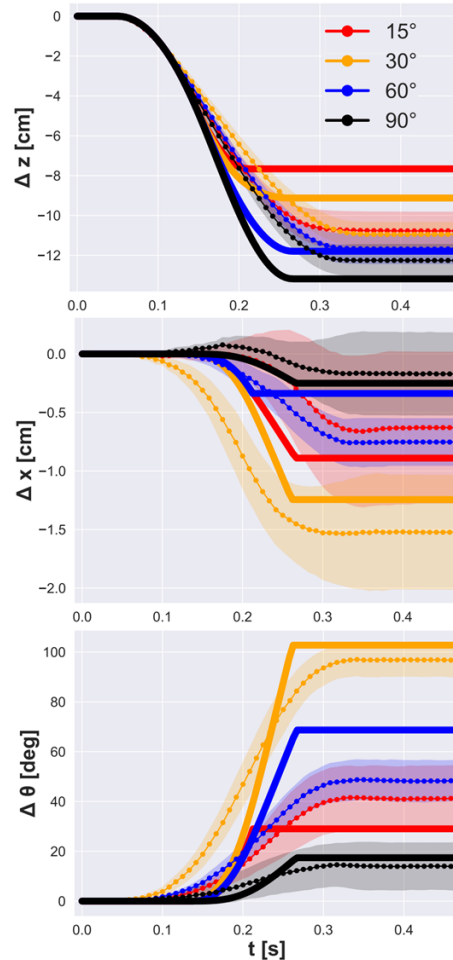

Fig. S5. Model prediction vs experimental results. The lines made of square dots represent the output of Eqs. 3-5, while the dotted curves are the corresponding experimental results (see Fig. 2 of the main text). The legend represents the initial angular position, $\theta(t = 0)$, of the attached grain.

breaking the granular force chains, thus ceasing to experience a resistive force from it Note that adding an inertial drag term will not remove the bouncing, it just dampens the oscillations. Using this approximations, the model reduces the amount of free parameters.

The output of the Eqs. 3-5 is shown in Fig. S5.

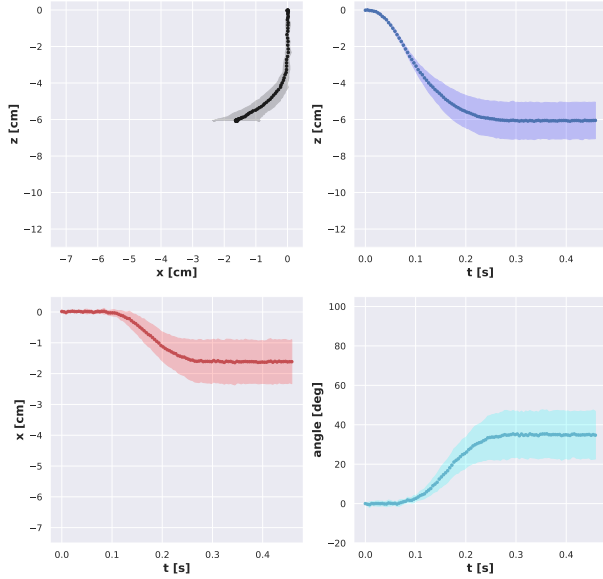## SETTLING OF A ROUGH CYLINDER

Fig. 6S. Experimental results of the penetration of the Rough cylinder. Results are averages over 10 repetitions of each experiment. The colored bands represent the respective standard deviation.

In addition to the Janus and the ScarFace Janus cylinders, other experiments were carried out to study the effect of small irregularities in the surface of cylindrical objects on their penetration into a granular bed. As mentioned earlier when discussing the analytic model in the main text, a further behavior could be expected from a cylindrical intruder with evenly glued grains across the surface, which we will call Rough cylinder.

As predicted by the model, the experimental results showed that the Rough cylinder penetrates much less than the Janus cylinder in the granular bed (Fig. 6S). Lateral displacement and rotation are also greatly reduced, a fact stemming from the intruder's restored symmetry. The fact that it rotates somewhat could be due to a slight difference in the distribution of the grains between the halves of the Rough cylinder (note that the grains were randomly selected and stuck to the cylinder).

DENSITY JANUS CYLINDER

Although the main focus of the work is the study of roughness-related asymmetries, an intruder with different material density
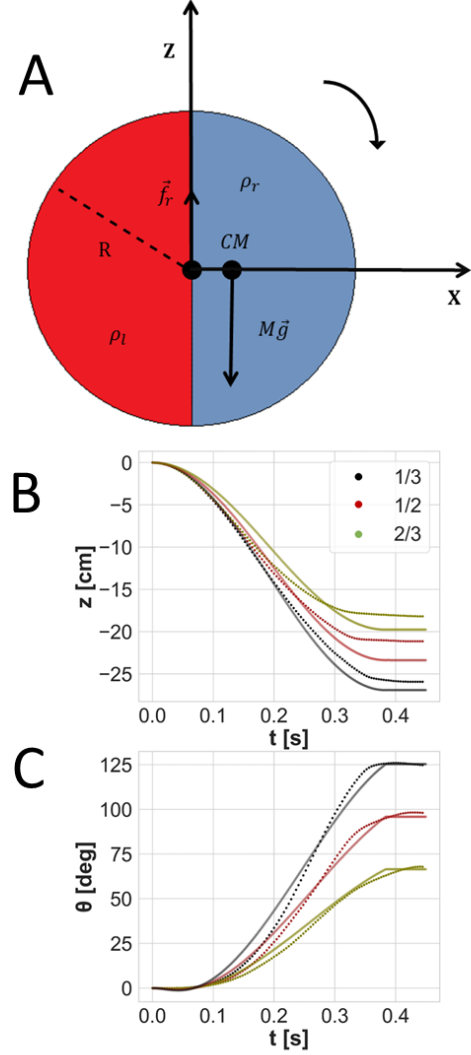

Fig. S7. Expected behavior of a Density Janus cylinder. (A) Schematic representation of the front view of a cylinder with different densities. ρ_l and ρ_r are the densities of each half, f_r is a resistive force similar to that of Katsuragi-Durian, CM_l, CM_r and CM_b, represent the location of the center of mass of the left side, the right side, and the whole body, respectively. (B-C) Time evolution of intruder penetration and rotation angle for different density ratios. Dotted and solid curves represent simulations and model results, respectively.

for each half is also a type of *Janus intruder*. In this section we analyze a simple case: a cylindrical intruder with inhomogeneous density as shown in Fig. S7 (A). The difference in density results in the rotation of the intruder in the direction of the denser half, as shown in the figure. Applying this condition to the Katsuragi-Durian penetration law, we obtain:

$$\frac{V(\rho_r + \rho_l)}{2}\ddot{z} = -\frac{V(\rho_r + \rho_l)}{2}g - kz \qquad (7)$$

$$\ddot{\theta} = \frac{16(\rho_r - \rho_l)}{3\pi R^3(\rho_r + \rho_l)}\left(\frac{g\pi R^2}{2} + \frac{2kz}{h(\rho_r + \rho_l)}\right), \qquad (8)$$

where ρ_r and ρ_l are the densities of the right and left side respectively. R, h and V are the radius, height and volume

of the cylinder, respectively (same as the experimental values). To solve Eqs. 7 and 8, the same considerations were assumed as in the model presented in the main text for the Scarface Janus cylinder. k is used as a fitting parameter to reproduce the DEM simulations results for the values of $\rho_d/\rho_i = 1/3, 1/2$ and $2/3$. After fitting the data we obtained $k = 108\,\mathrm{kgs}^{-2}$.

Due to the simplicity of the physical system analyzed, we were able to obtain a dynamic model that is easy to understand and that allows us to explain the intruder's rotation by density differences in its volume. As we can see in the Fig. S7 (B)-(C), it approximately reproduces the results of the DEM simulations.

The first important characteristic to point out, which completely differentiates this system from the Janus cylinder described in the main text, is that its surface is smooth, which implies that the rotation is caused by the imbalance associated to the mass difference, i.e, while the rotation in the case of the Janus cylinder is produced by a difference in the resistive force acting on each half, the rotation of the Density Janus cylinder is caused by a displacement of the center of mass due to the different densities ρ_r and ρ_l, as shown in Fig. S7 (A). The larger the difference in density between each half, the greater the displacement of the CM of the intruder, and therefore, the greater the net torque exerted by the resistive force, as we can observe in Fig. S7 (C). Note that in this case (Density Janus cylinder), the symmetry of the force chains is not broken and, consequently, there is no lateral displacement of the intruder, so all our analysis focuses on rotation.

The density averages used for each distribution are: $\overline{\rho_{1/3}} = 1800\,\mathrm{kg/m}^3$, $\overline{\rho_{1/2}} = 1350\,\mathrm{kg/m}^3$ and $\overline{\rho_{2/3}} = 1125\,\mathrm{kg/m}^3$, respectively, while the experimental density of the intruder is $\rho_{exp} = 1236\,\mathrm{kg/m}^3$. The higher the average density, the more the intruder penetrates into the granular bed, as shown in Fig. S7 (B).

SETTLING OF A HUMAN SKULL

Taken to a physicist's extreme, the Scarface intruder works as a minimalist model of a human skull consisting in a sphere with one tooth attached. Indeed, an actual human skull with its mandible removed can be seen as a Janus intruder due to its lack of symmetry when viewed from the side. This suggests that a human skull released into granular matter may follow a non-trivial motion, eventually involving both rotation and horizontal motion. We have demonstrated that a human skull also shows strong tilting and lateral shift as it settles in a bed of polystyrene particles in a way consistent to our Janus intruders.

Here we quantify the penetration process of a human skull released from the free surface of a granular bed made of very light granular material. As in the case of the Janus intruders experiments, the granular material was contained into a Hele-Shaw cell –now obviously of larger dimensions. Due to the complex shape of the skull, it was not possible

to track the center of mass of the intruder or measure its rotation by directly filming it from the side of the cell, so a thin steel rod was attached perpendicularly to the upper part of the cranium, and filmed from various positions during the penetration process.

The skull intruder was facilitated by the "Felipe Poey" Museum of Natural History (University of Havana), with catalog number 32.00314. The object –from unknown origin– has belonged to their osteological collection for more than 30 years. The skull has a cranial breadth of 13.5 cm, and length of 21.5 cm. A steel rod of 1 mm diameter and 30 cm length was attached perpendicularly to the bone surface, in such a way that the extrapolation of the rod axis passed by the Center of Mass of the skull. The cranium, initially hanging from the steel rod, was released electromagnetically, as in the case of the cylindrical intruders. The CM was located by hanging the skull from two different points (one at a time) and crossing the two lines down from each support point. The Hele-Shaw cell for these experiments was 39 cm length, 20 cm width and was filled up to a height of 30 cm, following a protocol analogous to the one for the experiments with cylindrical intruders, which resulted in a packing fraction of 0.69 ± 0.01. The granular material was the same as the one used in the latter case, as well as the video camera, resulting in a spatial resolution of 62.0 ± 0.2 pixels/mm.

Fig. S8(A) shows a photograph of the human skull under scrutiny: the maxilla with some remaining teeth, as well as the nasal and zygomatic bones can be taken as a "rougher" surface, when compared to the relatively smooth occipital and parietal bones located at the back of the skull. In spite of many other differences, these prominent characteristics resemble our Janus intruders. The sequence of snapshots shown in Fig. S8(B) demonstrates that the analogy may not be wrong: as the object is released into the granular medium in "head-up" position, the skull rotates counterclockwise, and laterally moves into the space near its "smoother" side (rotation and lateral motion within a plane perpendicular to the paper where shown to be negligible). Fig. S8(C) shows the relatively complex trajectory of the skull's center of mass, as expected considering its rather complex geometry as compared to our cylindrical Janus intruders. Figure S8 (D) quantifies the rotation mentioned above. Curiously, the total rotation angle of 40 degrees is very near the one observed in the case of a $\theta_{grain} = 15^o$ ScarFace Janus cylinder, but we are unable to explain it at the present stage. Fig. S8(E) shows snapshots of the skull penetration when released "head-down". Fig. S8(F) indicates a slight lateral motion, which seems to reflect the fairly smooth and symmetric bottom of the intruder in this experiment. However, Fig. S8(G) reveals a total rotation larger tan 15 degrees. One may speculate that the clockwise rotation in both "head-up" and "head-down" experiments could be influenced not only by the shape of the skull, but also by its inhomogeneous density distribution. A further surprising element here, is that the vertical penetration in the "head-up" experiments is substantially larger than that in the "head-down" experiments.
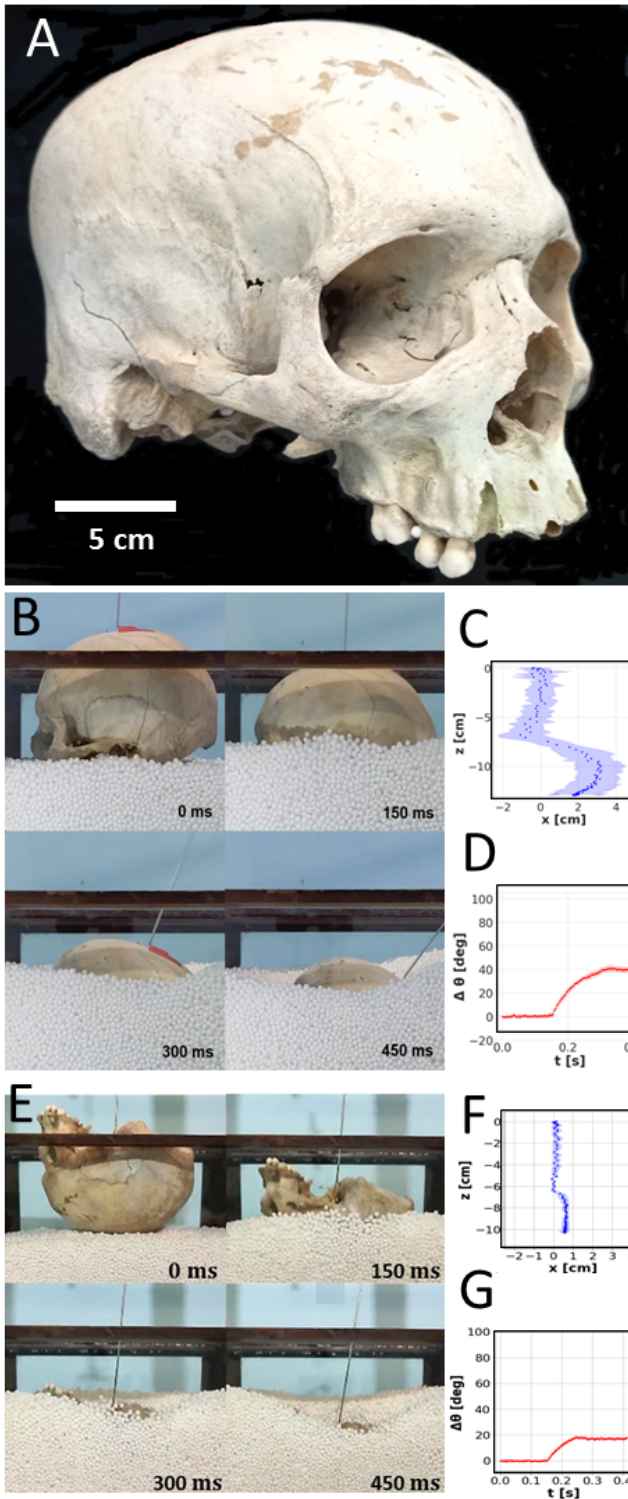
Fig. S8. Asymmetric penetration of a skull. (A) Photograph of the skull used in the experiments (B) Snapshots of the head-up penetration process taken from the experiment. (C) Trajectory of the skull's CM in head-up penetration. (D) Rotation angle vs. time for the head-up penetration (E) Snapshots of the head-down penetration process taken from the experiment (F) Trajectory of the skull's CM in head-down penetration. (G) Rotation angle vs. time for the head-down penetration. Rotation angle of the skull. The dotted lines in graphs from (C), (D), (F) and (G) are averages over 10 repetitions of each experiment; the colored bands around them represent the fluctuations of the experimental values

.

"Imperfect bodies sink imperfectly when settling in granular matter": Description of the supplementary videos.

Video adf623_Supplementary Movie_mov1_seq1_v1.mp4: Penetration of a stone into and air-fluidized bed of sand.

Video adf623_Supplementary Movie_mov2_seq2_v1.mp4: Penetration of a Janus cylinder into an air-fluidized bed of sand.

Video adf623_Supplementary Movie_mov3_seq3_v1.mp4: Penetration of a Janus intruder into a granular bed made of expanded polystyrene beads.

Video adf623_Supplementary Movie_mov4_seq4_v1.mp4: Penetration of a 15-degrees Scarface Janus cylinder into a granular bed made of expanded polystyrene beads.

Video adf623_Supplementary Movie_mov5_seq5_v1.mp4: Penetration of a 30-degrees Scarface Janus cylinder into a granular bed made of expanded polystyrene beads.

Video adf623_SupplementaryMovie_mov6_seq6_v1.mp4 Penetration of a 60-degrees Scarface Janus cylinder into a granular bed made of expanded polystyrene beads.

Video adf623_SupplementaryMovie_mov7_seq7_v1.mp4 Penetration of a 90-degrees Scarface Janus cylinder into a granular bed made of expanded polystyrene beads.

Video adf623_SupplementaryMovie_mov8_seq8_v1.mp4 Penetration of a human skull into a granular bed made of expanded polystyrene beads.